Supporting Information

High Energy Efficiency and Stability for Photoassisted Aqueous Lithium-Iodine Redox Batteries

Georgios Nikiforidis[1,2], *Keisuke Tajima*[3], *and Hye Ryung Byon*[1,2,4]*

[1]Department of Chemistry, Korea Advanced Institute of Science and Technology (KAIST), 291 Daehak-ro, Yuseong-gu, Daejeon 34141, Republic of Korea

[2]Byon Initiative Research Unit (IRU), RIKEN, 2-1 Hirosawa, Wako, Saitama 351-0198, Japan

[3]Emergent Functional Polymer Research Team, RIKEN Center for Emergent Matter Science (CEMS), 2-1 Hirosawa, Wako, Saitama 351-0198, Japan

[4]KAIST Institute NanoCentrury, 291 Daehak-ro, Yuseong-gu, Daejeon 34141, Republic of Korea

E-mail: *hrbyon@kaist.ac.kr*

Figure S1. Electrodeposition of γ-FeOOH on FTO. (a) Schematic view of a three-electrode electrochemical cell. (b) Charge curve for two-minute electrodeposition at 1.2 V vs Ag/AgCl (4 M KCl) and 78 °C in an aqueous solution containing 0.02 M $FeCl_2$ (pH 4.1). The deposition process resulted in (1) the oxidation of Fe^{2+} to Fe^{3+} (2) followed by the precipitation of Fe^{3+} as amorphous ferric oxyhydroxide (γ-FeOOH). (c) Amount of the deposited amorphous γ-FeOOH calculated from Faraday's law ($Q = n \times F \times N$).

(a)

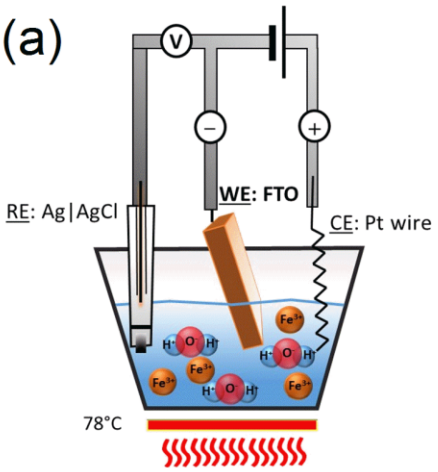

(b)

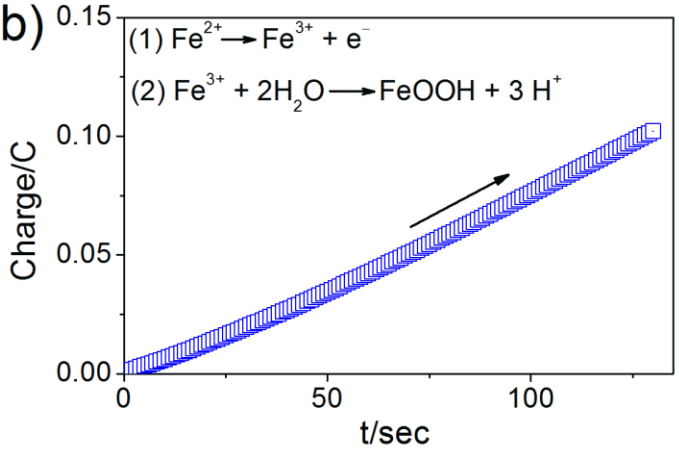

(c)

Total Charge / C	Number of moles	Mass of FeOOH / mg
0.102	1.06×10^{-6}	0.09

Figure S2. Schematic illustrations (top row), optical (middle) and SEM (bottom) images of FTO coated glass substrates that are as received (left column), after electroplating (center) and after annealing (right). The films consisting of small nanoparticles cover the FTO after electrodeposition (γ-FeOOH) and annealing (α-Fe_2O_3), depicting transparent light orange and deep orange color, respectively.

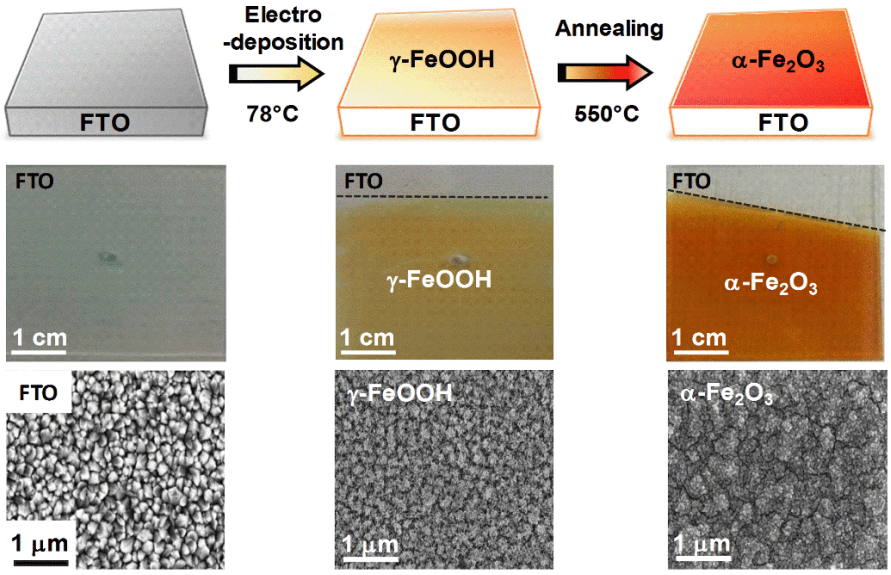

Figure S3. Characteristics of as-prepared hematite film on FTO substrate. (a) XRD pattern of α-Fe_2O_3. The asterisk (*) peaks arise from the FTO substrate (JCPDS # 77-0452). (b) Raman active modes (A_{1g} and E_g) of hematite. Raman inactive E_u appears possibly due to the presence of defects. [1] (c) XPS of Fe 2p binding energy region. Fe $2p_{3/2}$, $2p_{1/2}$ and satellite are attributed to Fe^{3+} in hematite. [2] (d) Tauc plot stemmed from UV-visible spectrum (inset) with baseline of a bare FTO. The Tauc plot indicates an indirect optical band energy of 2.15 eV.

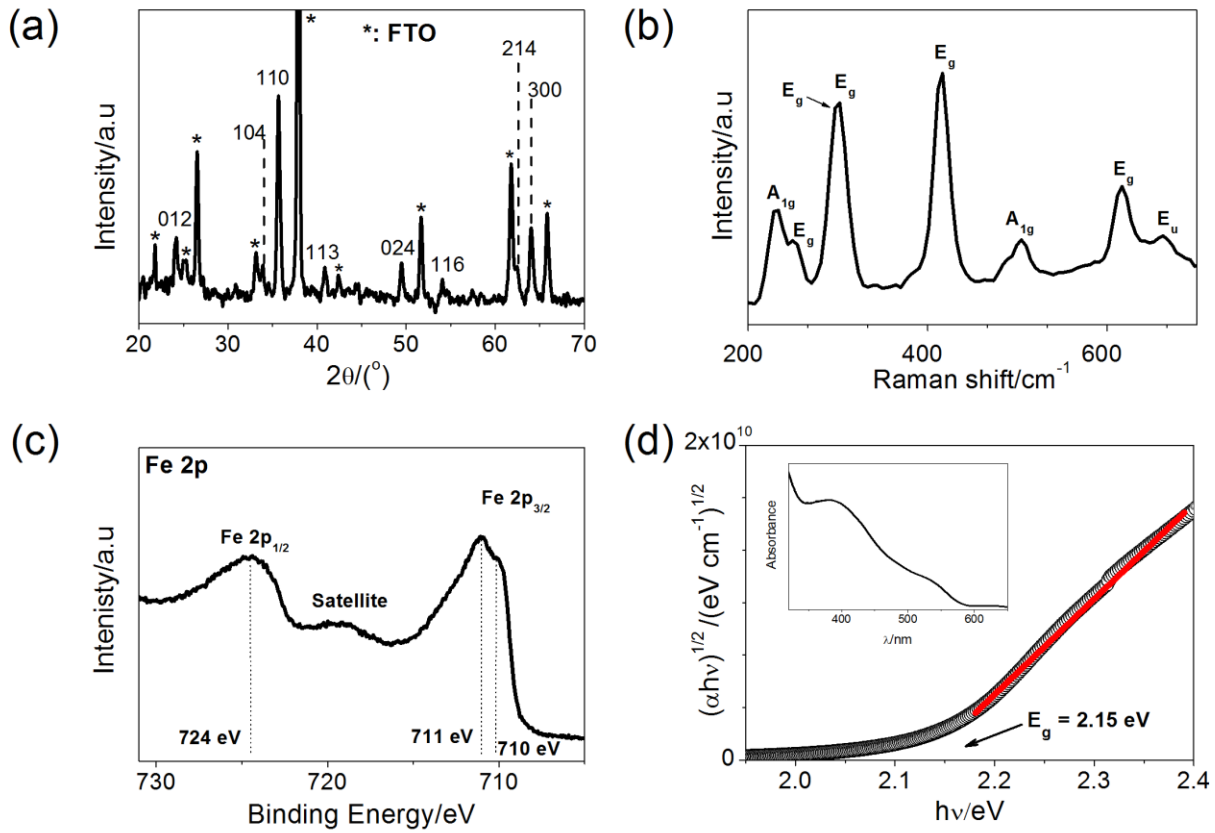

Figure S4. Cross-sectional SEM image of hematite film (ϕ=90 nm) on FTO coated glass (ϕ=700 nm).

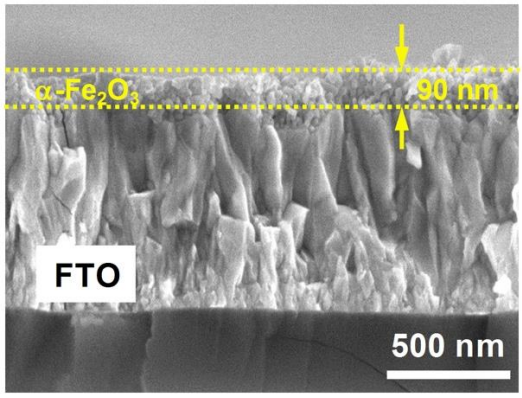

Figure S5. OCV (open circuit voltage) and temperature monitoring of aqueous Li–I_2 cell with chopped illustration for 50 h. The aqueous catholyte consists of 1 M KI, 0.03 M LiI and 0.08 M I_2 (pH 7.9). Temperature measurement was carried out using a thermistor in contact with the hematite/FTO substrate.

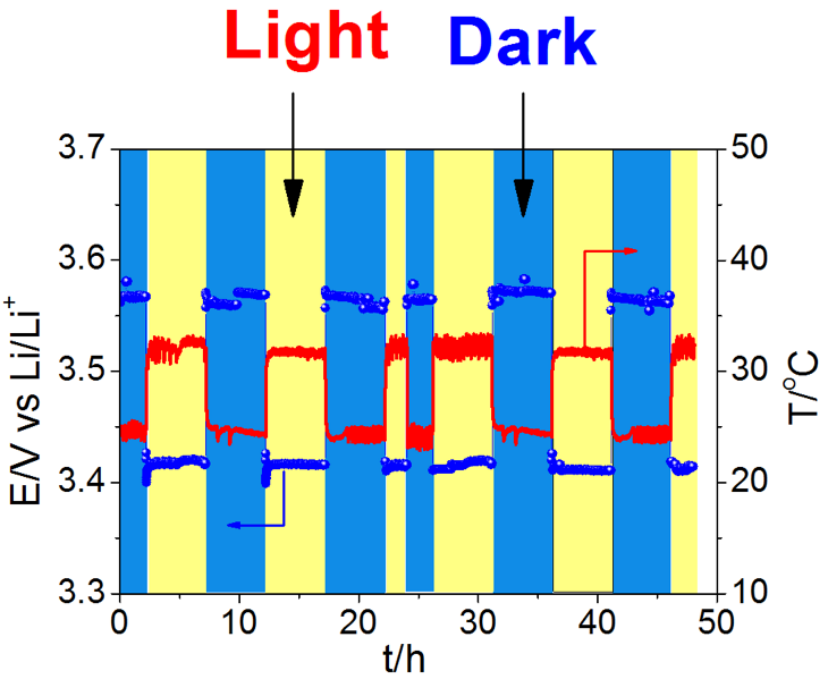

Figure S6. Equivalent circuit of Li-I_2 aqueous cell (Figure 1c). The use of constant phase elements (Q) reflects the porosity and the consequent non-ideal behavior of the capacitive elements denoted by α.[3] R_1 represents the uncompensated cell resistance including electrolyte at the negative electrode, wiring and the separator while R_2 (mid-frequency region) is a parallel circuit of a constant phase element (Q) that embodies the transfer resistance and diffusion of the charge carriers between hematite and I^-/I_3^- catholyte. R_3 (low frequency region) denotes the charge transport at the hematite/FTO interface.

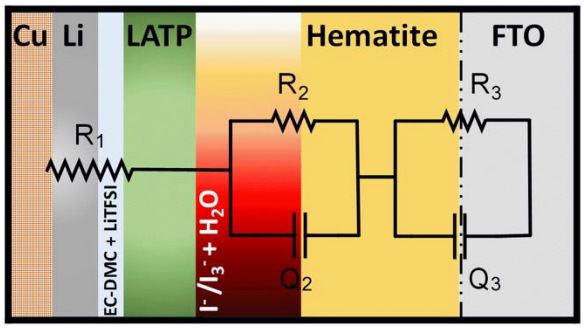

Table S1. EIS fitting results at OCV (Figure 1c) using a catholyte containing 1 M KI, 0.03 M LiI and 0.08 M I_2 (pH 7.9). Under dark conditions, R_2 and R_3 are larger than in light conditions due to the absence of photogenerated charge carriers. The constant phase coefficient alpha (α) values lingered between 0.7~0.8 supporting the non-ideal capacitor behavior of circuits 2 (R_2, Q_2) and 3 (R_3, Q_3).

Equivalent Circuit	R_1 [$\Omega.cm^2$]	R_2 [$\Omega.cm^2$]	Q_2 [$F.s^{(\alpha-1)}$]	R_3 [$k\Omega.cm^2$]	Q_3 [$F.s^{(\alpha-1)}$]
Light (32 °C)	88.2	122.8	1.4×10^{-7}	7.4	3.7×10^{-6}
Dark (25 °C)	97.9	183.4	8.4×10^{-8}	17.6	2.3×10^{-6}
Dark (32 °C)	91.3	166.3	7.1×10^{-8}	15.4	2.7×10^{-6}

Figure S7. Polarization resistance plots of the aqueous Li-I_2 cell (conditions: ±15 mV from OCV at a sweeping rate of 0.166 mV s^{-1}) in aqueous catholyte of 1 M KI, 0.03 M LiI and 0.08 M I_2. Sunlight suppresses polarization resistance by a factor of 2–3, that is, $R_p = (\Delta V/\Delta i) = 2.0\ k\Omega.cm^2$ in light vs 6.3.$k\Omega$ cm^2 and 4.2 $k\Omega.cm^2$ in dark at 25 and 32 °C, respectively (Table S2). Increased temperature under dark conditions (32 °C) led to a somewhat decreased resistance possibly due to the enhanced ionic mobility of the aqueous electrolyte.

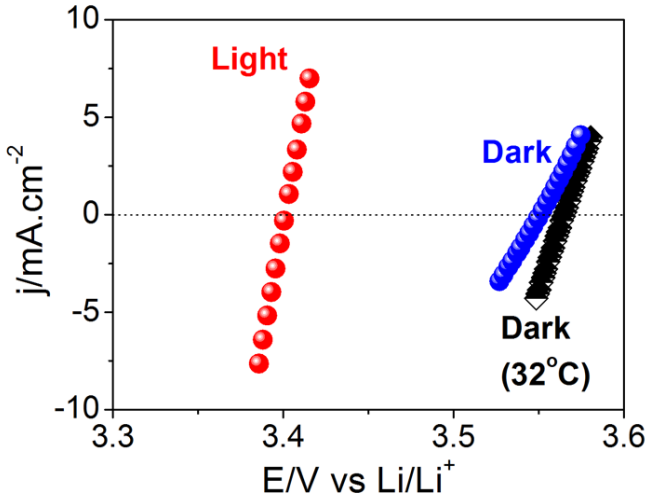

Table S2. Tafel extrapolation (Figure 1d) and polarization resistance (Figure S7) results normalized by the geometric surface area of the hematite photocathode (0.64 cm^2) exposed to the aqueous catholyte. Higher exchange current densities ($j_{0\ Tafel}$) in the presence of light are consistent with the decreased polarization resistance values (R_p), indicating photogeneration of charge carriers.

	E_{ocv}	$j_{o\ Tafel}$	$j_{o\ Pol.\ resistance}$	R_p
	[V vs Li/Li^+]	[μA cm^{-2}]	[μA cm^{-2}]	[kΩ.cm^2]
Light	3.4	15.4	12.9	2.0
Dark	3.55	4.0	4.2	6.3
Dark (32 °C)	3.57	4.6	6.2	4.2

Figure S8. Photoresponse on aqueous Li-I_2 cell in 1 M KI, 0.03 M LiI and 0.08 M I_2 at a current density of 0.075 mA cm^{-2}. First charge was carried out under dark and the following seven cycles (2^{nd} ~8^{th}) under illumination. (a) Charge voltage profiles for all 8 cycles. (b) Coulombic efficiency (η_C), (c) Voltaic efficiency (η_V) and (d) Energy efficiency (η_E) according to cycling. The cell was fully discharged prior to every charge process. The average η_C, η_V and η_E under illumination is 98.8%, 95.6% and 95.4%, respectively.

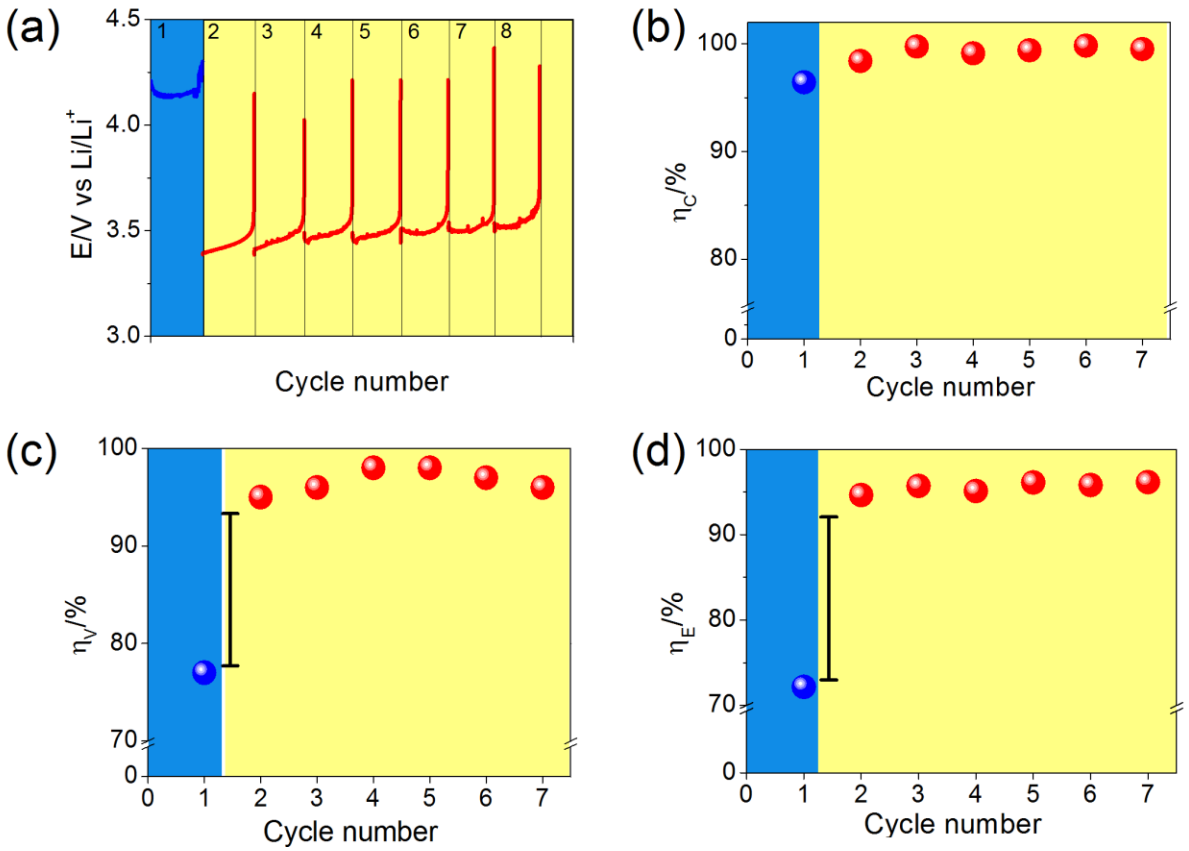

Figure S9. Temperature effect of LATP separator. **(**a) Nyquist plot of LATP impedance using symmetric cell (Cu|Au|LATP|Au|Cu cell, surface $area_{LATP}$ = 1.4 cm^2) under dark. The measurements were carried out over a frequency range of 1 MHz to 1 Hz and an amplitude of 10 mV. At high frequencies the small semicircle represents the grain boundary resistance of LATP (R_b) while the intercept of the semicircle with the real axis at the medium to low frequency range relates to the bulk resistance of LATP (R_{gl}).[4] Clearly, elevated temperature (32 °C) reduces R_{gl} by a factor of 1.35. Insets show schematic views of equivalent circuit and LATP cell configuration. (b) Discharge-charge curves under dark and elevated temperature (32 °C, blue area) at a current rate of 0.05 mA cm^{-2} in aqueous catholyte of 1 M KI, 0.03 M LiI and 0.08 M I_2 and two cycles under light (yellow area) as a comparison. (c) Corresponding specific capacity comparison upon all deep discharge-charge cycles.

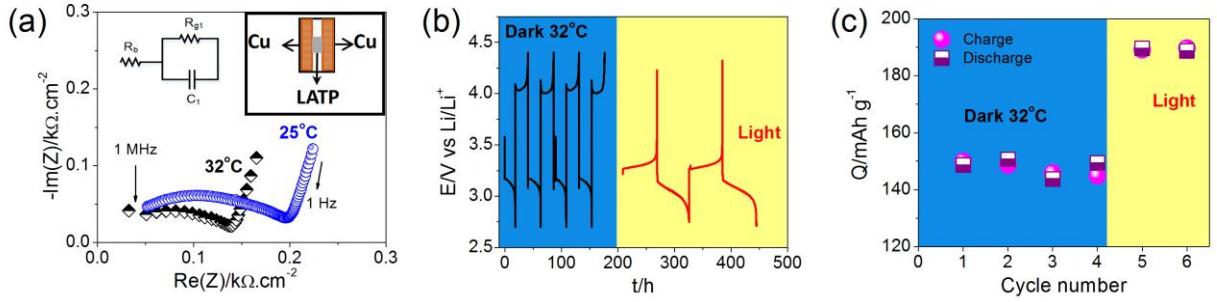

Figure S10. Cyclic performance of the aqueous Li–I_2 cell in 1 M KI, 0.03 M LiI and 0.08 M I_2 at current rates of 0.1 and 0.05 mA cm^{-2} (Figure 3a–b). (a) Deep discharge-charge cycles under dark (blue area) and light (yellow area). (b) Comparison of voltage and capacity curves at a current rate of 0.05 mA cm^{-2}.

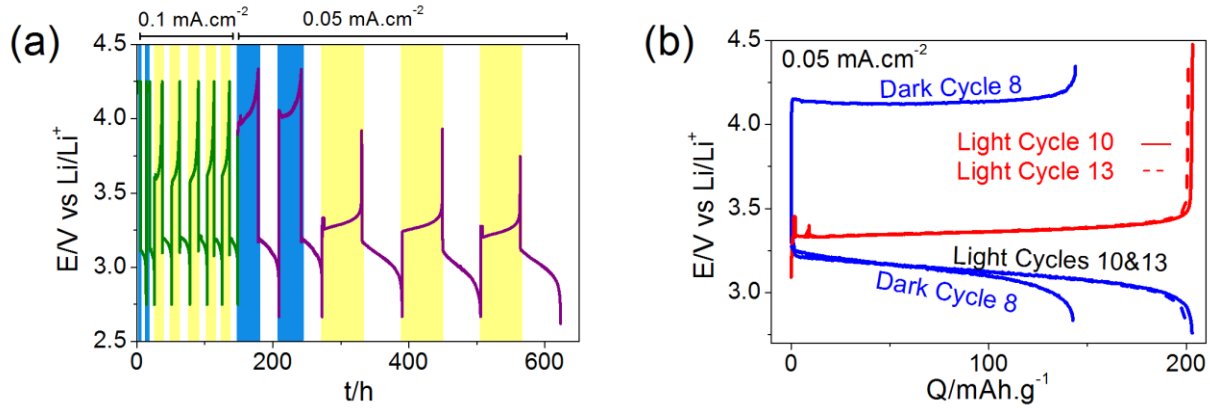

Figure S11. Areal power density profiles of the aqueous Li–I_2 cell in 2 M KI and 0.2 M I_2. (Areal power density was evaluated, based on the geometric available surface area of the hematite photoelectrode). The cell was fully discharged prior to measurement.

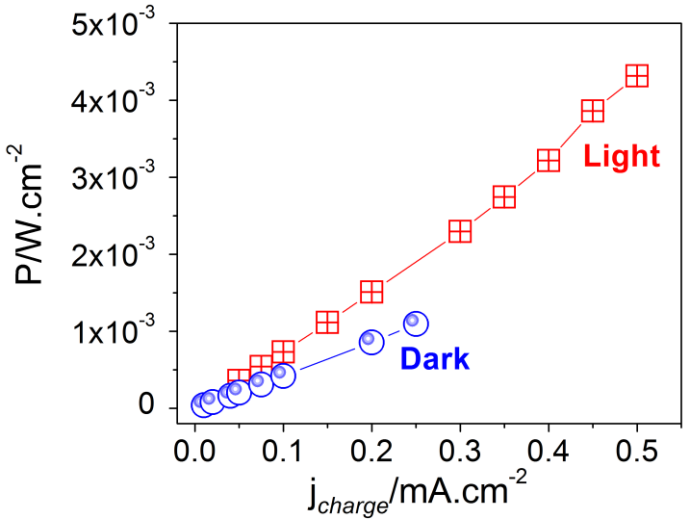

Figure S12. Characteristics of hematite photoelectrode before (black) and after 30 cycles (pink, Figure 3e–f) using (a) XRD, (b) Raman and (c) top-view SEM images of hematite film.

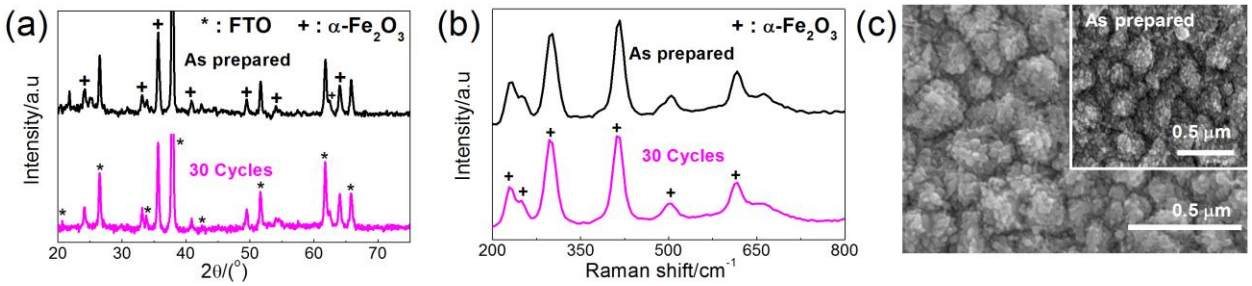

Figure S13. Comparison between hematite photoelectrode (red for light and blue for dark) and carbon electrodes (grey) for the aqueous Li–I_2 cell in 1 M KI, 0.03 M LiI and 0.08 M I_2. (a) Tafel plot at a sweeping rate of 0.5 mV s^{-1}, (b) polarization resistance plot (conditions: ±15 mV from OCV at a sweeping rate of 0.166 mV s^{-1}) and (c) deep discharge and charge curves for the carbon electrode at a current rate of 0.075 mA cm^{-2}. The OCV, $j_{o\ Tafel}$, $j_{o\ Pol.\ resistance}$ and η_E for the carbon electrode is 3.61 V (close to the expected equilibrium voltage of I^-/I_3^- (~3.55 V)), 23.6 μA cm^{-2}, 22 μA cm^{-2} and 96%, respectively.

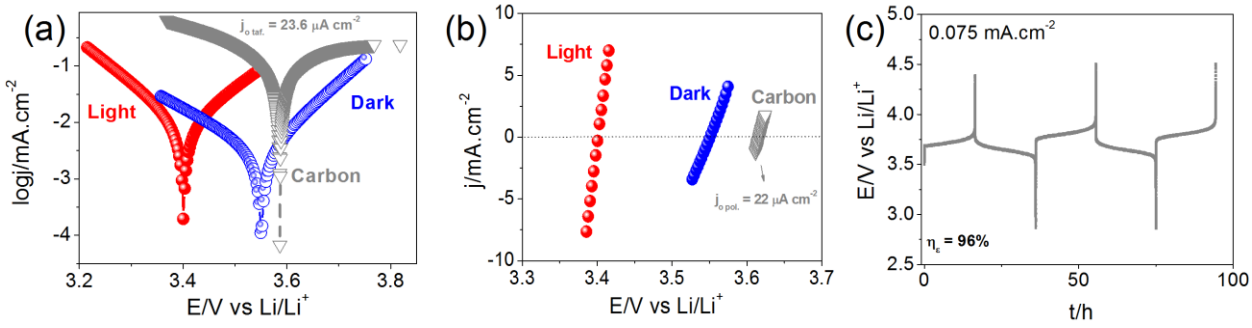

Figure S14. Characteristic of hematite photoelectrode with sputtered gold layer (ϕ=2 nm, hematite/Au/FTO substrate). (a) XRD pattern of hematite with gold film underlayer. For the XRD plot, the small peak at 2θ = 44.2° is attributed to cubic gold 200 reflection.[5] (b) Comparable UV-visible spectra of hematite films with and without Au film. The calculated optical band energy of hematite/Au/FTO substrate was ~2.18 eV. (c) EIS measurements at OCV in aqueous Li–I_2 cells with hematite/Au/FTO under light and dark conditions (Table S3) at a frequency range from 600 kHz to 100 mHz and an AC amplitude of 10 mV. The aqueous catholyte was comprised of 1 M KI, 0.03 M LiI and 0.08 M I_2. With illumination, a huge improvement in the resistance is demonstrated. Insets show the equivalent circuit (left) and zoomed-out high frequency region Nyquist plot. (d) Photoresponse of the aqueous Li–I_2 cell with hematite/Au/FTO at OCV under light and dark. The OCV under illumination lingers at 3.42 V according to the optical band gap while under dark the potential obeys the Nernst principle and reaches at 3.6 V. An overall voltage gain of 180 mV is evidenced.

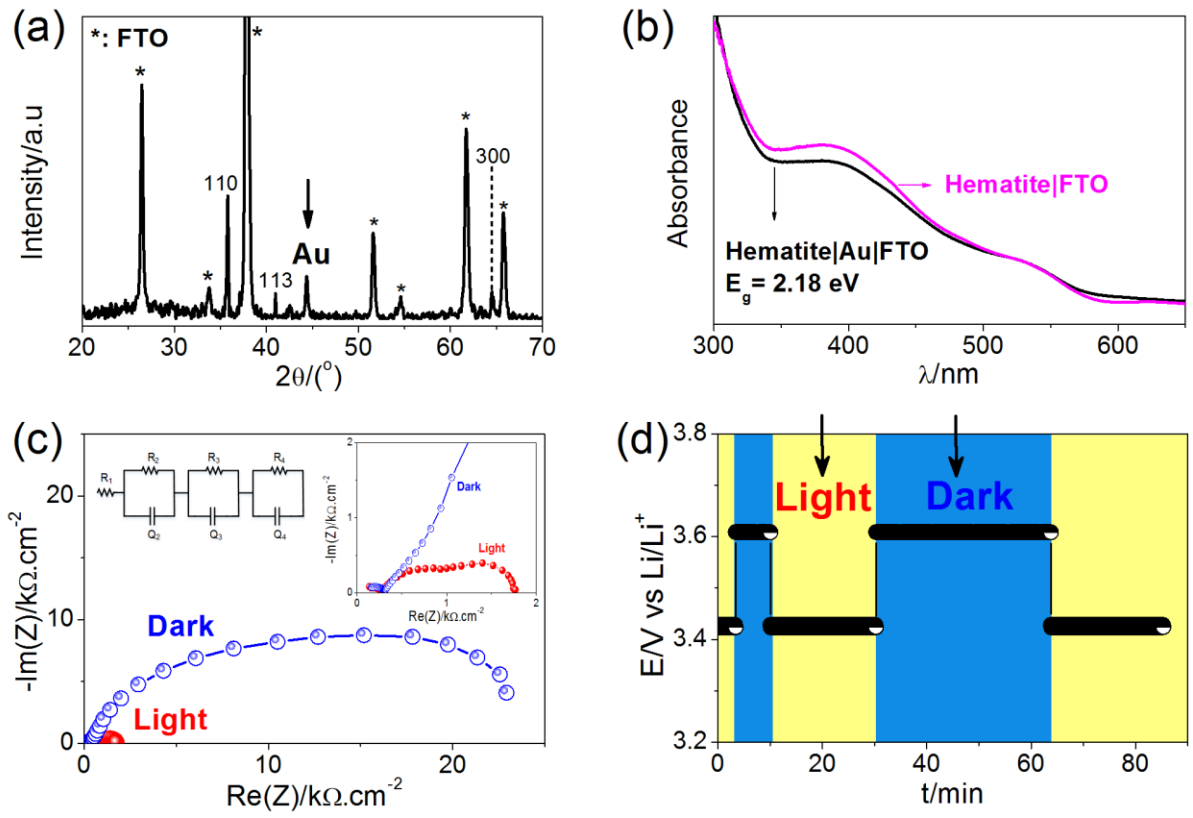

Table S3. EIS fitting results under light and dark conditions for aqueous Li-I_2 cells using a hematite/Au/FTO substrate (Figure S14c). R_1 and R_2 are resistances at negative electrode/electrolyte (R_1 in Table S1) and hematite/catholyte (R_2 in Table S1), respectively. The introduction of a gold underlayer was accompanied by the addition of a circuit element (R_3,Q_3) describing the Au/FTO interface, while (R_4,Q_4) represents the hematite/FTO interface. The constant phase coefficient (α) values ranged between 0.30 and 0.95.

Equivalent Circuit	R_1 [$\Omega.cm^2$]	R_2 [$\Omega.cm^2$]	Q_2 [$F.s^{(\alpha-1)}$]	R_3 [$\Omega.cm^2$]	Q_3 [$F.s^{(\alpha-1)}$]	R_4 [$k\Omega.cm^2$]	Q_4 [$F.s^{(\alpha-1)}$]
Light	100.5	131.7	2.21×10^{-6}	21.54	4.0×10^{-7}	2.7	3.2×10^{-6}
Dark	121.2	214.2	9.1×10^{-6}	16.86	8.6×10^{-6}	23.5	7.8×10^{-6}

References

1. Jorand Sartoretti, C.; Ulmann, M.; Alexander, B. D.; Augustynski, J.; Weidenkaff, A., Photoelectrochemical oxidation of water at transparent ferric oxide film electrodes. *Chem. Phys. Lett.* **2003,** *376*, 194-200.

2. Zong, X.; Thaweesak, S.; Xu, H.; Xing, Z.; Zou, J.; Lu, G.; Wang, L., A scalable colloidal approach to prepare hematite films for efficient solar water splitting. *Phys. Chem. Chem. Phys.* **2013,** *15*, 12314-12321.

3. Hirschorn, B.; Orazem, M. E.; Tribollet, B.; Vivier, V.; Frateur, I.; Musiani, M., Determination of effective capacitance and film thickness from constant-phase-element parameters. *Electrochim. Acta* **2010,** *55*, 6218-6227.

4. Hasegawa, S.; Imanishi, N.; Zhang, T.; Xie, J.; Hirano, A.; Takeda, Y.; Yamamoto, O., Study on lithium/air secondary batteries—Stability of NASICON-type lithium ion conducting glass–ceramics with water. *J. Power Sources* **2009,** *189*, 371-377.

5. Chew, C. K. T.; Salcianu, C.; Bishop, P.; Carmalt, C. J.; Parkin, I. P., Functional thin film coatings incorporating gold nanoparticles in a transparent conducting fluorine doped tin oxide matrix. *J. Mater. Chem. C* **2015,** *3*, 1118-1125.